scientific reports

OPEN

Global spatiotemporal analysis of interactions between urban heat islands and extreme heat waves

Johnny Guo[1], Xuhui Lee[2] & Keer Zhang[2,3]✉

Extreme heat waves (HWs), defined here as periods when daily maximum temperature exceeds the 98th percentile for three or more consecutive days, pose a significant threat to public health. The extreme heat risk is particularly relevant to urban residents due to the urban heat island (UHI) effect and its synergistic interactions with HWs in some cities. Previous research on the interactions between UHI and HWs has focused on a single city or region, and both positive and negative interactions have been reported. The global patterns of interactions between UHI and HWs across various climate backgrounds, as well as their underlying mechanisms, remain unclear. Here, we simulate the global urban heat island intensity (UHII) from 1985 to 2013 using the Community Land Model (CLM). By conducting a global-scale analysis of interactions between UHII and HWs, we diagnose their spatial and diurnal patterns across different regions and climate zones. To identify and explain the key contributors to the UHI-HW interactions, we employ machine learning models (CatBoost) and the SHapley Additive exPlanations (SHAP) framework to quantify the contributions of local energy flux, climate background, and land surface characteristics. UHI-HW interaction is quantified as the difference between UHII during heatwave (HW) days and non-heatwave (NHW) periods. We find that the UHI-HW interaction, which peaks at 6 AM local solar time (LT), is more positive at night than during the day. We identify net longwave radiation as a strong indicator of the interaction, while humidity emerges as a key driver, alongside contributions from sensible heat flux and wind speed. However, the influence of these factors varies across different Köppen–Geiger climate zones. Our study provides new insights into the complex interaction between UHIs and heat waves, with implications for urban climate adaptation strategies in a warming world. The machine learning-based approach offers a novel method for attributing the spatial variability in UHI heat wave interactions to specific biophysical variables.

Keywords Heat wave, Urban heat island, Surface evaporation, Surface energy balance, Surface biophysical driver

The urban heat island (UHI) effect, a phenomenon characterized by elevated temperatures in urban areas compared to their surrounding rural areas, is a concern exacerbated by the escalating effects of global warming and rapid urbanization. When compounded by heat waves (HWs), this effect is particularly worrisome, further enhancing the adverse effects of extreme heat on urban infrastructure, public health and labor productivity[1–3]. A better understanding of the interaction between UHI and HW may help inform effective mitigation and adaptation strategies.

A considerable body of research exists on UHI-HW interactions[4]. Heatwaves can modulate the spatial and temporal dynamics of the UHI through surface energy balance modifications, altered air flow, and changes in anthropogenic heat emissions. While many studies document synergistic relationships between UHI and HW events, others have not found such reinforcing effects. Most studies are limited to single cities or specific geographical regions[5–12]. Cities with different climate backgrounds and land surface characteristics may experience diverse UHI-HW interactions. A global study will provide a more comprehensive understanding of their patterns and underlying mechanisms. Moreover, many studies rely on satellite-derived land surface temperatures to examine UHIs, which, while offering wide coverage and temporal consistency, do not directly reflect the thermal conditions experienced by people within urban areas[7,13]. The Canopy Urban Heat Island, measured using air temperature, is more consistent with the thermal environment experienced by urban

[1]Choate Rosemary Hall, Wallingford, CT 06492, USA. [2]School of the Environment, Yale University, New Haven, CT 06511, USA. [3]High Meadows Environmental Institute, Princeton University, Princeton, NJ 08544, USA. ✉email: kz7693@princeton.edu

populations, making it a more pertinent indicator of heat stress and its direct impact on public health and thermal comfort[14].

This study addresses these research gaps by conducting a global-scale analysis of UHI-HW interactions using 2-m air temperature. We first characterize UHI-HW interactions' global spatial and temporal patterns, identifying their variability across climate zones and throughout the day. Using a machine learning model and the SHapley Additive exPlanations (SHAP) framework, we quantify the relative importance of biophysical variables influencing UHI-HW interactions across different regions. In this study, we use the term 'interaction' to describe the modulation of UHI intensity by heat wave conditions (i.e., the difference in UHI intensity between HW and NHW periods). Our offline modeling approach isolates the response of urban and rural surface climate states to large-scale heat wave forcing, consistent with previous analyses[7].

Methods
Simulation setup
We use the *Community Land Model version 5 (CLM5)*, the land component of the *Community Earth System Model version 2 (CESM2)*[15], to simulate the global climate for urban and rural lands. CLM employs a sub-grid approach to represent land surface heterogeneity, partitioning each grid cell into up to five distinct land units: glacier, lake, urban, vegetated, and crop. The same atmospheric forcing drives all sub-grid units within a single grid cell, but their specific parameterizations simulate their near-surface climates. In particular, urban climate is explicitly modelled as a single-layer urban street canyon, consisting of roof, sunlit and shaded walls, pervious and impervious lands[16]. We use the CLM 5.0[17] Satellite Phenology mode, which uses satellite-derived data to prescribe vegetation characteristics. We ran the simulation with a 0.9° latitude $\times$ 1.25° longitude resolution from 1985 to 2013, driven by atmospheric forcing from the Global Soil Wetness Project Phase 3 Version 1, which is bias-corrected[17]. A constant urban land cover in 2015 from Gao and O'Neill[18] and a present day (circa-2000) urban property dataset from Jackson et al.[19] are used to prescribe the urban extent, the morphology, radiative, and thermal properties of each urban region. CLM has been widely used to simulate urban heat island across different climate zones[13,20]. Its performance has been extensively validated against flux tower observations, site observations, and satellite data[13,20–22], showing good performance in simulating the magnitude, spatial patterns, and diurnal variations of air temperature UHI, surface UHI, and the surface energy balance (see Supplementary Methods for detailed descriptions on model validation). The simulation was spun up for 20 years, driven by atmospheric forcing cycled between 1991 and 2010 to ensure the equilibrium of the land initial states.

This study focuses on heatwaves (HWs), and thus, our analysis focuses on the summer hot months, June to August for the Northern Hemisphere and December through February for the Southern Hemisphere. We utilize hourly data, specifically from 08:00 to 16:59 LT (9 h), to represent daytime conditions, while nighttime is defined as local hours between 20:00 and 4:59 LT (9 h). Hours 17:00–19:59 and 05:00–07:59 LT are excluded from day/night aggregates but are included in the hourly analyses. Among 55296 (288×192) global grid cells, 3648 cells have the urban portion and are studied.

Definition of heat waves and UHI interaction
Definitions of heat waves vary across studies[4,23]. This research defines heat waves for each grid cell based on its corresponding rural 2-m air temperature data. Specifically, a heat wave (HW) for a given location is identified as:

$$\mathrm{HW} = \{day|T_{r,m} > T_{98}\} \text{ for 3 or more consecutive days} \tag{1}$$

where maximum daily rural temperature $T_{r,m}$ is the area-weighted mean of daily maximum 2-m air temperature of vegetated and cropland units in a grid cell, and T_{98} is the 98th percentile. This percentile value is based on the daily maximum in the summer, as defined previously, between 1985 and 2013 (a total of 2668 days for grids in the Northern Hemisphere and 2610 days for grids in the Southern Hemisphere). This approach was applied to 29 years of data, categorizing days into HW days and non-heatwave (NHW) days for each studied grid. Globally, the average length of HW is 4.24 ± 2.11 days (mean ± 1 s.d.). The average lengths of HW in different climate zones range from 3.82 to 4.26 days, as detailed in Supplementary Table S1.

The UHI is given by:

$$\mathrm{UHI} = T_\mathrm{u} - T_\mathrm{r} \tag{2}$$

where T_u and T_r are the area-weighted mean of hourly 2-m air temperature for urban and rural subgrids, respectively. To quantify the interactions between heat wave and UHI effect, we calculate the UHI difference (ΔUHI) between HW and NHW days, matching by the hour. The ΔUHI at a specific hour (h) and a given year (y) is defined as:

$$\Delta\mathrm{UHI}_{\mathrm{d,h}} = \mathrm{UHI}_{\mathrm{hw,d,h}} - \mathrm{UHI}_{\mathrm{nhw,h,y}} \tag{3}$$

where $\mathrm{UHI}_{\mathrm{hw,d,h}}$ is the UHI of date d at hour h. Hence, there is one interaction value for every hour in HW periods. Outside HW days, there is no interaction value. $\mathrm{UHI}_{\mathrm{nhw,h,y}}$ is the average of all NHW UHI at hour h for year y. Hence, for a given year y, $\mathrm{UHI}_{\mathrm{nhw}}$ consists of 24 data points, each representing the average UHI at a specific hour of the day. We allow these 24 points to vary across different years to control year-to-year climate shifts.

Machine learning model

We employed a gradient-boosting machine learning approach (CatBoost) to identify the key drivers of UHI-HW interactions using an hourly panel dataset of 6.1 million observations pooled across all urban locations. The model predicts ΔUHI—the difference in urban heat island intensity between heatwave and non-heatwave conditions—using biophysical features derived from the surface energy balance. To ensure interpretability, we integrated SHapley Additive exPlanations (SHAP), which quantify each feature's contribution to the predicted UHI enhancement during heatwaves (see Supplementary Methods for detailed methodology).

The surface energy balance equation provides the theoretical foundation for our feature engineering:

$$R_{\mathrm{n}} + Q_{\mathrm{A}} = \mathrm{H} + \lambda \mathrm{E} + \mathrm{G} + Q_{\mathrm{s}} \tag{4}$$

where R_{n} represents net all-wave radiation (comprising shortwave K_{n} and longwave L_{n} components), Q_{A} denotes anthropogenic heat, H the sensible heat flux, λE the latent heat flux, G the ground heat flux, and Q_{s} the heat storage[24]. To avoid multicollinearity and maintain interpretability, we excluded λE (highly correlated with H) and retained H as the sole turbulent flux term.

Our feature engineering employs a two-tiered differentiation structure: δ denotes urban-rural spatial differences, while Δ represents heatwave-non-heatwave temporal differences. Through iterative feature selection and validation, we identified 11 key predictors from an initial set of 38 biophysical variables (Supplementary Table S2). The final features comprise: net longwave radiation ($\Delta\delta L_{\mathrm{n}}$), specific humidity ($\Delta\delta q_{\mathrm{a}}$ and Δq_{a}), 10-m wind speed ($\Delta \mathrm{U}_{10}$), ground heat flux ($\Delta\delta G$), sensible heat flux (ΔSH), soil moisture in the top 10 cm ($\Delta\Theta_{10\mathrm{cm}}$), net shortwave radiation (ΔK_{n}), and anthropogenic heat from air conditioning ($\Delta \mathrm{AH}_{\mathrm{ac}}$).

Model performance was evaluated using 10-fold cross-validation, achieving a Root Mean Square Error (RMSE) of 0.0987 ± 0.0007 °C and R^2 = 0.96, demonstrating robust predictive capability. The stable performance across folds confirms that our climate zone-specific attribution results reflect physical relationships rather than statistical artifacts. Detailed model parameters, feature selection methodology, and validation procedures are provided in the Supplementary Methods.

Results and discussion

Spatiotemporal patterns of UHI-HW interactions

Global diurnal cycle and spatial distribution

The global simulation results show a clear diurnal pattern for the synergy of UHI and HWs. The ΔUHI exhibits a peak of 0.37°C at around hour 05 to 06 LT (local solar time) and a trough of -0.04°C at around 09 to 10 LT. It also shows a local peak at around 19 LT (Fig. 1). Aggregating to the diurnal level, we found the nighttime average ΔUHI 0.27 ± 0.23°C (mean ± 1 s.d.) is higher than its daytime counterpart 0.02 ± 0.22°C. Statistical analysis confirms that these patterns are robust, with significant ΔUHI ($p < 0.05$) observed in over 96% of urban grid cells with more than 10 HW days globally (Fig. 2). The results are consistent with previous findings, where positive[12,25–27], insignificant[28], and negative[8,29–31] ΔUHI were reported, depending on the regions studied.

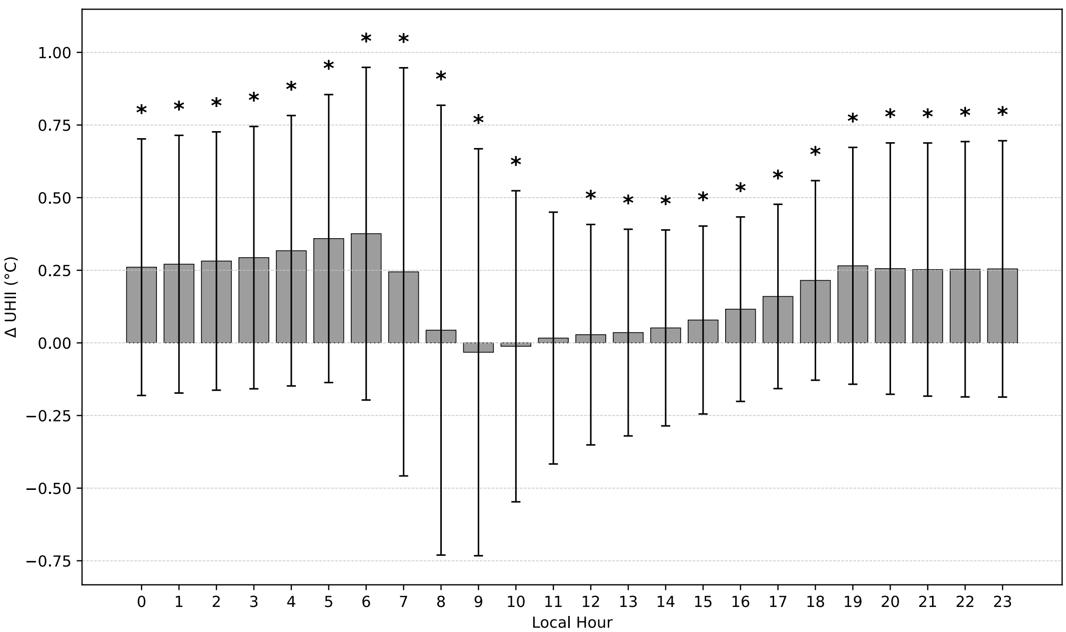

Fig. 1. Diurnal Variations of ΔUHI for the studied 3648 urban grid cells. Y axis is ΔUHI($^{\circ}$C). Bars represent the mean, and error bars indicate (±) one standard deviation across urban grid cells. Asterisks (*) above the bars indicate hours where ΔUHI is significantly different from zero (Wilcoxon signed-rank test with Bonferroni correction, $p < 0.05/24$).

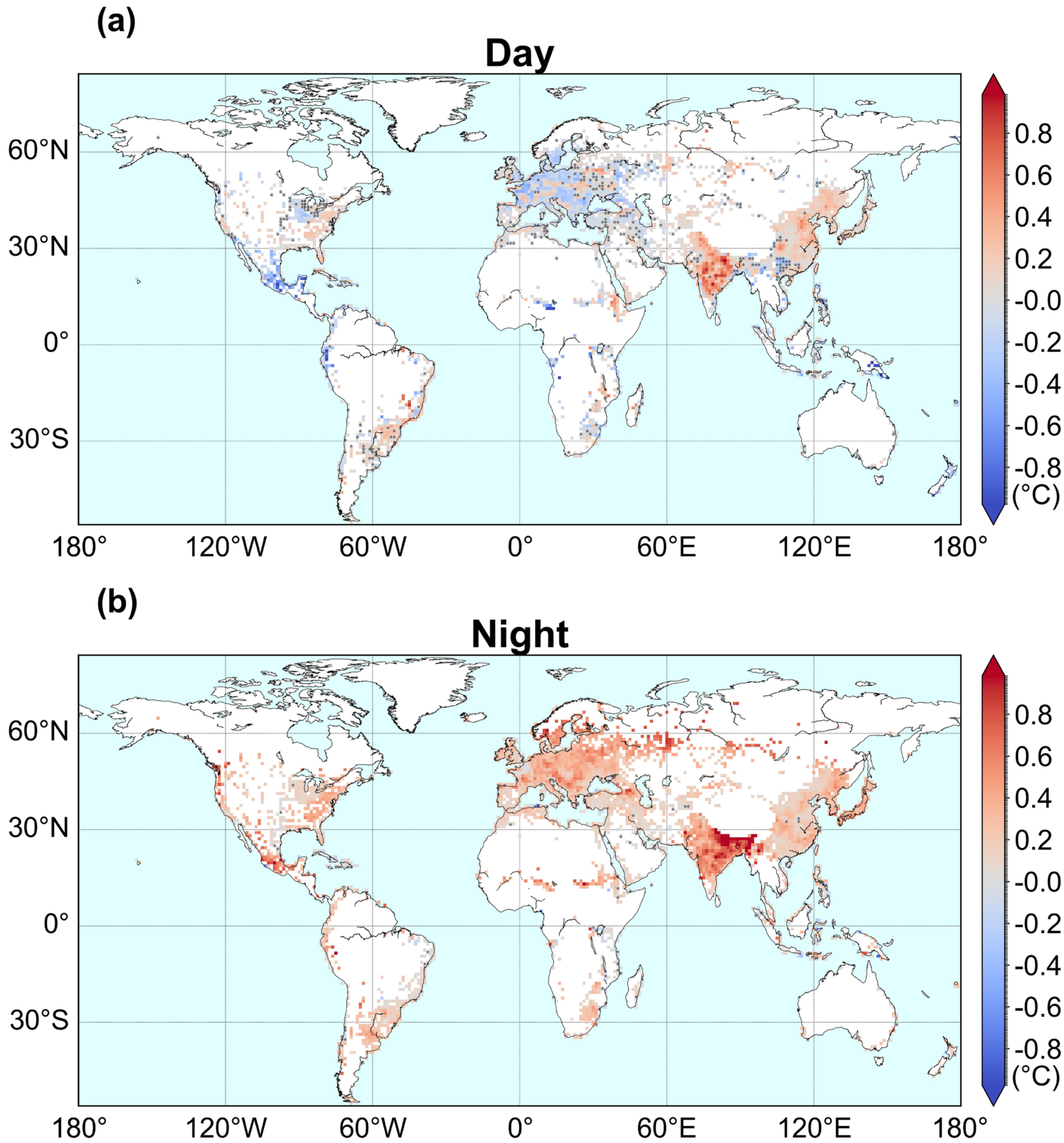

Fig. 2. Geographical distributions of ΔUHI. Panels show the average ΔUHI for (**a**) daytime and (**b**) nighttime. Asterisks (*) grid cells indicate statistically insignificant ΔUHI ($p >= 0.05$, Wilcoxon signed-rank test). The color scale represents the strength of the interaction in degrees Celsius (°C). *Note*: CLM5 represents urban areas as sub-grid land tiles. While the ΔUHI are plotted for the entire grid cell for visualization, they are urban-scale results; the continuous ΔUHI spatial pattern does not indicate physical urban continuity.

Figure 2 reveals spatial patterns in ΔUHI globally. During the day, notable spatial heterogeneity is observed. Negative or near-neutral interactions are widespread across global coastal areas; major humid mid-latitude agricultural zones, such as the US Corn Belt and Western and Central Europe; and low-latitude tropical regions, including the Southeast Asia, and southern Mexico. In contrast, distinct positive synergies are clustered within the Indo-Gangetic and North China Plains. At night, the interaction is much stronger and the spatial pattern is more uniform, with the most pronounced hotspot (0.8°C) over northern India. Neutral or slightly negative signals are limited to isolated equatorial grids.

Variations across climate zones

The geographically-bound patterns observed in Fig. 2 show notable alignment with the Köppen-Geiger climate classification map[32]. For example, a distinct negative interaction over the US Corn Belt matches the boundaries of the Dfa (Humid continental) climate zone. Similar correspondence is evident in regions such as Western Europe, Northeast China, Northern India, Southeast Asia, and the Southeastern United States. The observed

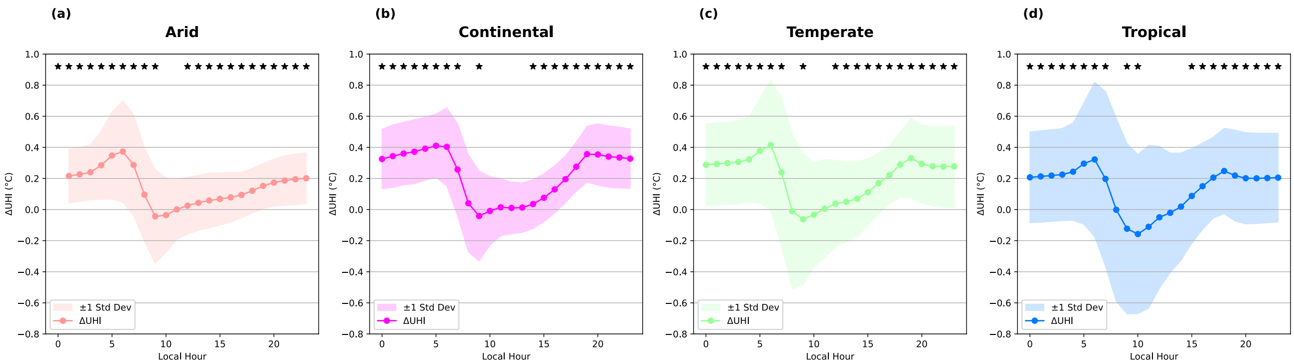

Fig. 3. Diurnal Cycle of ΔUHI across Köppen-Geiger Climate Zones. Line plots showing the mean hourly ΔUHI(°C) for (**a**) Arid, (**b**) Continental, (**c**) Temperate, and (**d**) Tropical climate zones. Shaded areas represent ±1 standard deviation around the mean. Asterisks (*) above each curve indicate hours where ΔUHI is significantly different from zero (Wilcoxon signed-rank test with Bonferroni correction, $p < 0.05/96$).

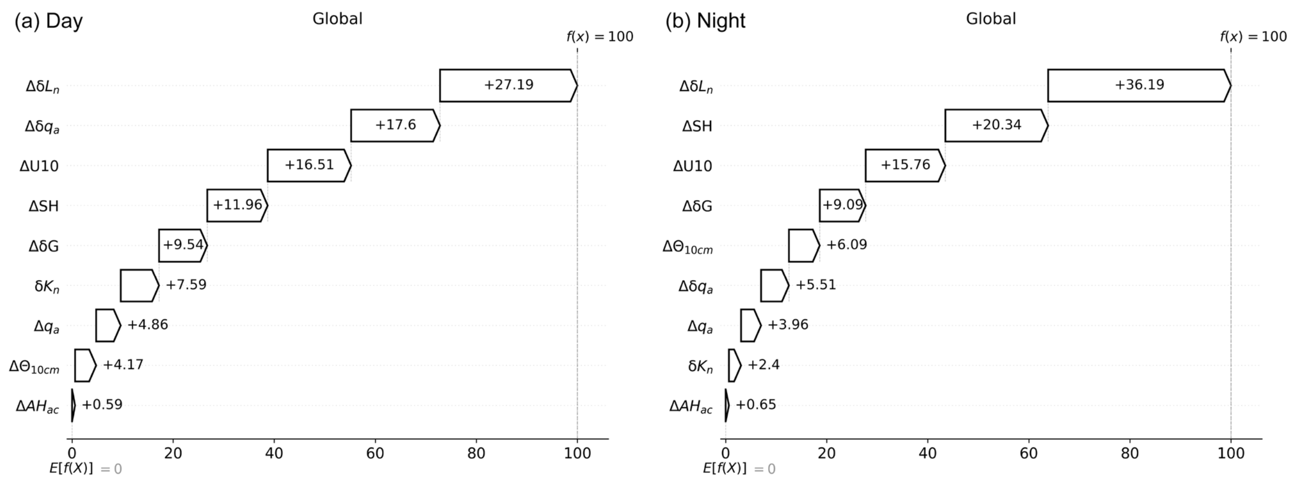

Fig. 4. SHAP-based analysis of feature contributions to the predicted ΔUHI, derived from the CatBoost model trained in this study. The waterfall plots depict each feature percentage contribution to the model's prediction for daytime (**a**) and nighttime (**b**) conditions.

agreement between UHI-HW interaction patterns and established climate zones indicates the importance and utility of conducting subsequent analyses stratified by climate classifications.

Across the four major Köppen-Geiger climate zones[32] analyzed in this study, the ΔUHI climate zone curves exhibit similar diurnal patterns but differ in the interaction magnitudes (Fig. 3). The continental climate zone has the most significant positive peak synergy, while tropical climates have the lowest. Synergy is strongest in the Continental zone, followed by the Temperate zone, especially at night, while the Tropical zone exhibits the highest variance in ΔUHI for both daytime and nighttime (Supplementary Fig. S1). In this study, we excluded locations belonging to the Polar Köppen-Geiger climate zone.

Regional variability

The high variance observed in tropical regions reflects contrasting local conditions. While the Indian subcontinent shows strong positive UHI-HW synergy, Mexico and Central America display negative interactions. This regional heterogeneity, driven primarily by differences in humidity and ground heat flux patterns during heatwaves, is analyzed in detail in the Supplementary Information (Figs. S1–S3).

Attribution and mechanisms of UHI-HW interactions

Overview of global influential factors

The SHAP waterfall plots (Fig. 4) and summary plots (Fig. 5) provide complementary insights into feature contributions. The waterfall plots quantify the cumulative contribution of each feature to a specific model prediction, while the summary plots indicate the distribution and directionality of individual feature impacts (positive or negative influence on ΔUHI). It is important to distinguish between statistical association and physical causation when interpreting these results. While SHAP values quantify the contribution of each feature to the model's prediction, they represent statistical associations rather than causal drivers.

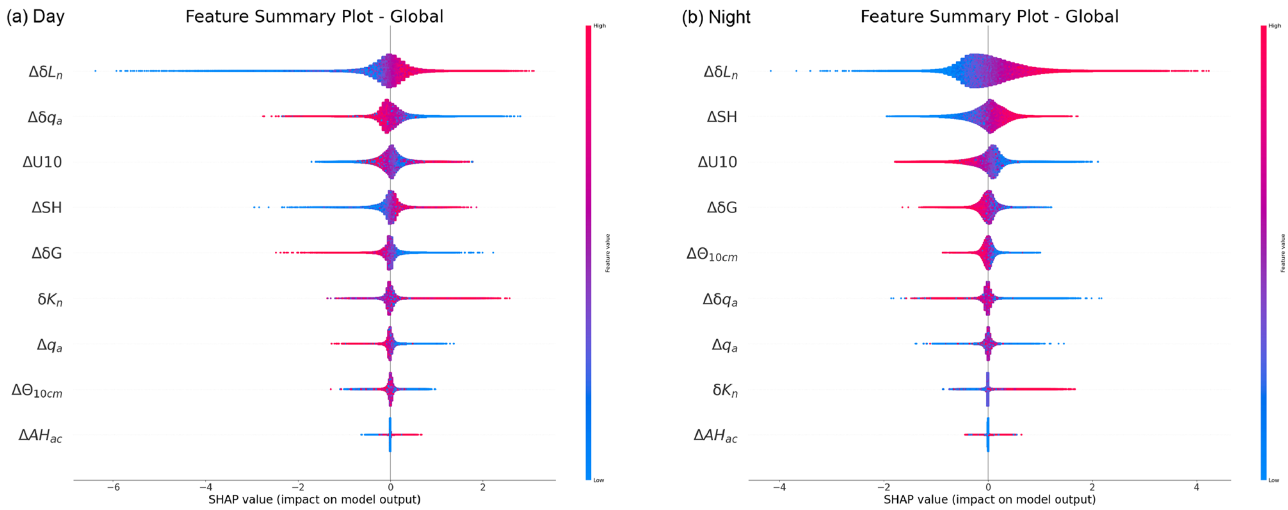

Fig. 5. SHAP summary plots showing the distribution and magnitude of feature impacts. **(a)** daytime, (**b**) nighttime. Each point represents a single instance; the horizontal position indicates the SHAP value (positive values denote an increase in predicted $\Delta\mathrm{UHI}$, negative a decrease); the color represents the original feature values (blue: low, red: high).

Fig. 4 shows $\Delta\delta L_\mathrm{n}$ as the most important indicator of ΔUHI (27.19% by day; 36.19% by night), and SHAP values increase with $\Delta\delta L_\mathrm{n}$ (Fig. 5), indicating positive comovement. Humidity contributes more in daytime, with $\Delta\delta q_\mathrm{a}$ and Δq_a combining for 22.46%; the summary plot indicates a negative association of $\Delta\delta q_\mathrm{a}$ and Δq_a with ΔUHI (lower $\Delta\delta q_\mathrm{a}$ corresponds to higher positive SHAP). ΔSH ranks next (11.96% day; 20.34% night) and displays a positive association. ΔU10 is important at night (15.76%) and shows a negative comovement, with higher ΔU10 linked to lower SHAP, potentially due to higher wind speed consistent with near surface heat dispersion at night; the daytime association is weak. $\Delta\delta G$ contributes at single-digit levels and shows weak negative comovement. δK_n is minor with weak positive comovement. Declines in $\Delta\Theta_{10\mathrm{cm}}$ align with higher SHAP, consistent with a negative association, and $\Delta\mathrm{AH}_\mathrm{ac}$ has small contribution with a weak positive association.

A more granular temporal analysis, presented in Fig. 6, is important for understanding these dynamics throughout the full diurnal cycle. It illustrates the global hourly cycle of mean SHAP value contributions for these variables. Understanding these specific hourly contributions and transition periods is essential for linking variable influence to the observed overall ΔUHI peaks (e.g., 5 to 6 AM) and troughs (e.g., 9 to 10 AM) identified in Fig. 1.

For instance, net longwave radiation ($\Delta\delta L_\mathrm{n}$) exhibits a positive contribution to the UHI-HW interaction, peaking around 06 to 07 LT and again with a smaller peak around 19 to 20 LT. In contrast, its contribution becomes negative during midday. The influence of specific humidity ($\Delta\delta q_\mathrm{a}$ and Δq_a) peaks in the late morning and midday. These detailed hourly patterns, which would be obscured if relying solely on the broader daytime and nighttime averages, are essential for understanding how each variable contributes to the direction of ΔUHI changes.

To understand the basis of these associations throughout the diurnal cycle, we examined two properties of each variable (detailed hourly analysis in Supplementary Fig. S4): its instantaneous level and its temporal change. First, for each hour, we link the sign and magnitude of the feature to its SHAP contribution. Second, we assess whether hour-to-hour changes in the feature are positively or negatively associated with concurrent changes in its SHAP contribution. For net longwave radiation ($\Delta\delta L_\mathrm{n}$), positive values correspond to larger positive SHAP contributions (Supplementary Fig. S4a), and increases in $\Delta\delta L_\mathrm{n}$ are associated with increases in SHAP during both day and night, consistent with Fig. 5. For specific humidity, the values of $\Delta\delta q_\mathrm{a}$ are mainly negative for all hours, while SHAP values are positive during the day and small during the night. In the late morning, increases (becoming less negative) of $\Delta\delta q_\mathrm{a}$ correspond to a decrease of SHAP contributions (Supplementary Fig. s4c), again consistent with Fig. 5 regarding the negative comovement relationship. Sensible heat flux (ΔSH) contributes positively during the day and negatively at night (Supplementary Fig. s4b), with SHAP contributions generally covarying with the feature values. The 10-m wind speed (ΔU10) contributes negatively at night, with SHAP contributions in a reverse relationship with the feature values. During the day, ΔU10 tends to contribute positively, although the value and SHAP association is weaker, as also seen in Fig. 5.

Net longwave radiation
The global attribution analysis identifies net longwave radiation $L_\mathrm{n} = L^\uparrow - L^\downarrow$ as a strong indicator of the UHI-HW interaction (Fig. 4), with SHAP values consistently increasing with δL_n (Fig. 5).

Upward longwave radiation is given by [33]

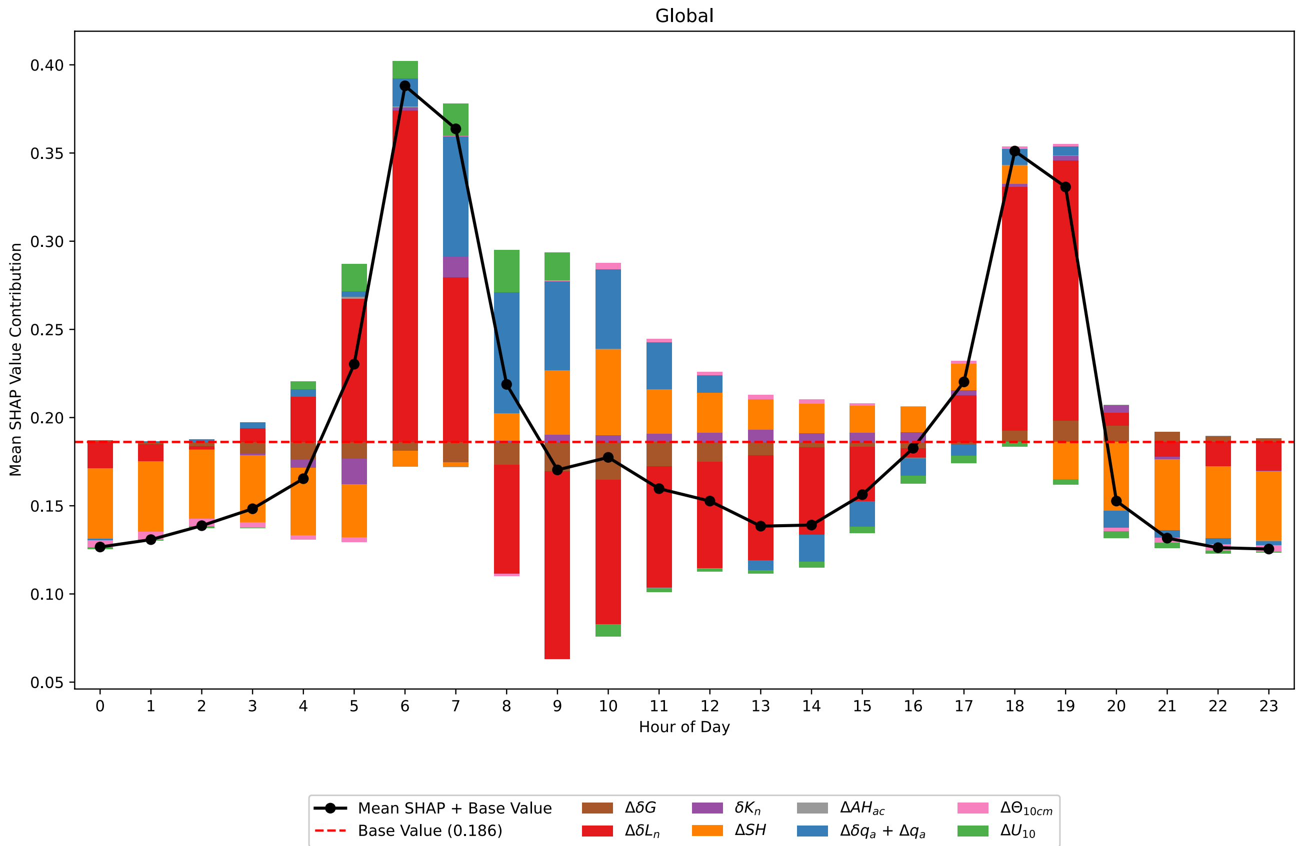

Fig. 6. Global hourly cycle of mean SHAP value contributions. The y-axis represents the mean SHAP value contribution ($^{\circ}$C). Features' SHAP displayed as stacked bars. The solid black line indicates the total model prediction (sum of all mean SHAP contributions plus the base value), while the red dashed line shows the model's base value (0.186°C). Contributions from individual features ($\Delta\delta L_{\mathrm{n}}$ (red), ΔSH (orange), $\Delta\delta q_{\mathrm{a}} + \Delta q_{\mathrm{a}}$ (blue), ΔU10 (green), $\Delta\delta G$ (brown), δK_{n} (purple), $\Delta\mathrm{AH_{ac}}$ (gray), and $\Delta\Theta_{10\mathrm{cm}}$ (pink)), as detailed in the legend, are plotted against LT.

$$L^{\uparrow} = \varepsilon\sigma T_{\mathrm{skin}}^4 + (1-\varepsilon)L^{\downarrow} \tag{5}$$

where ε is the surface emissivity, σ is the Stefan-Boltzmann constant, and T_{skin} is the skin temperature. Because CLM5 applies the same $L^{\downarrow}$ to urban and rural tiles, the urban-rural difference reduces to:

$$\delta L_{\mathrm{n}} = L_{\mathrm{u}}^{\uparrow} - L_{\mathrm{r}}^{\uparrow} \tag{6}$$

and consequently, $\Delta\delta L_{\mathrm{n}} = \Delta\delta L^{\uparrow}$. With constant emissivities, the heatwave-induced change in the urban-rural difference becomes:

$$\Delta\delta L^{\uparrow} = \varepsilon_{\mathrm{u}}\sigma\Delta\left(T_{\mathrm{u}}^4\right) - \varepsilon_{\mathrm{r}}\sigma\Delta\left(T_{\mathrm{r}}^4\right) + (\varepsilon_{\mathrm{r}} - \varepsilon_{\mathrm{u}})\,\Delta L^{\downarrow} \tag{7}$$

Comparing the diurnal cycles of $\Delta\delta L^{\uparrow}$ (Supplementary Fig. s6b) and $\Delta\delta T_{\mathrm{skin}}$ (Supplementary Fig. s6d) reveals similar shapes. The close temporal correspondence between $\Delta\delta T_{\mathrm{skin}}$ and $\Delta\delta L^{\uparrow}$ indicates that the emission difference (the first two terms of Eq. 7) is the primary factor associated with the diurnal pattern.

However, $\Delta\delta L^{\uparrow}$ shifts to negative values during midday, while $\Delta\delta T_{\mathrm{skin}}$ remains slightly positive (Supplementary Fig. s6d). This discrepancy corresponds to negative emission terms (the first two terms of Eq. 7) due to smaller ΔT_{skin} gaps during the day (Supplementary Fig. s6c) and smaller urban emissivity compared to that of rural ($\varepsilon_{\mathrm{u}} < \varepsilon_{\mathrm{r}}$; 0.73 vs 0.96) for surface data used in the study. The reflection term (the third term of Eq. 7) can be positive but is usually small. Hence, we observe overall negative $\Delta\delta L^{\uparrow}$.

At night, enhanced urban heat release leads to a large positive $\Delta\delta T_{\mathrm{skin}}$ (peaking around $+0.7^{\circ}$C; Supplementary Fig. s6d). The resulting strong emission difference corresponds to positive peaks in $\Delta\delta L^{\uparrow}$ and ΔUHI before sunrise (Figs. 1 and 6).

In conclusion, nighttime positive values reflect enhanced urban emissions associated with widened skin temperature differences. In contrast, midday negative values are potentially associated with smaller urban emissivity and smaller temperature gaps between urban and rural surfaces.

Humidity
Atmospheric moisture modulates the ΔUHI by governing the partitioning of incoming energy into latent and sensible heat fluxes. This study includes $\Delta\delta q_{\mathrm{a}}$ and Δq_{a} as model features to capture the spatial and temporal variation of specific humidity's impact on ΔUHI.

Consistent with the global feature-importance patterns (Fig. 4a), the urban-rural specific humidity contrast $\Delta\delta q_{\mathrm{a}}$ plays a leading role in daytime UHI-HW interactions, characterized by a strong negative association with ΔUHI (Fig. 5a). Physically, a negative $\Delta\delta q_{\mathrm{a}}$ signifies that the urban atmosphere becomes even drier relative to the rural atmosphere during a heatwave than under NHW conditions (Supplementary Fig. s4c). This widening moisture gap forces a greater proportion of excess energy into sensible heat in the urban environment, exacerbating the ΔUHI. The hourly analysis highlights specific diurnal dynamics, notably a sharp drop in $\Delta\delta q_{\mathrm{a}}$ and a corresponding increase in its positive SHAP contribution around sunrise (Supplementary Fig. s4c). This pattern aligns with the mechanism of overnight rural dew evaporation, which temporarily suppresses the morning rise in rural temperatures and thus increases ΔUHI[34].

Leveraging double-difference ($\Delta\delta$) metrics on humidity-related variables is an established methodology for isolating synergistic effects, as demonstrated through analytical models, observational data, and climate modeling[7,12,34,35]. The present study extends this framework globally by applying standardized Δ and $\Delta\delta$ diagnostics within a SHAP attribution framework, enabling direct comparison of moisture-driven mechanisms. Our global analysis strongly corroborates these foundational studies: the strong negative correlation between $\Delta\delta q_{\mathrm{a}}$ and ΔUHI confirms that widening urban-rural moisture contrasts during heatwaves, driven by differential evaporative responses and processes, are primary drivers of UHI-HW synergy.

The physical mechanisms identified by this study's attribution analysis, namely, amplified urban-rural moisture contrasts, drive ΔUHI and are supported by a diverse body of literature employing different methodologies across various geographic locations [6,11,27,28]. The convergence of findings from analytical models, single-site observations, regional climate modeling, and this global-scale machine-learning attribution validates the moisture contrast as a primary and globally relevant drivers of UHI-HW synergy.

Influence of background climate and weather conditions
The ΔUHI depends strongly on background climate and prevailing weather[20], and shows pronounced spatial heterogeneity (Fig. 2, Supplementary Fig. s1). Synergy is strongest in the Continental zone, followed by the Temperate zone, especially at night (Supplementary Fig. s1). Hotspots such as the Indo-Gangetic and North China Plains (nighttime ΔUHI > 0.8°C) reflect sharp urban–rural contrasts in surface properties and moisture availability (Fig. 2). To examine these regional variations, we partitioned CatBoost SHAP contributions across the four major Köppen–Geiger climate zones (Fig. 7).

Across all climates, net longwave radiation (L_n) is a strong indicator, with its contribution from daytime (25 to 30%) to nighttime (35 to 44%), underscoring the role of radiative cooling (Fig. 7). Secondary contributors vary with the climate's primary thermal regulation mechanism, specifically, whether the background climate is moisture-limited or moisture-rich.

Interactions regulated by moisture variability
In climates with sufficient background moisture, the UHI-HW synergy follows the humidity-driven mechanism described above, where specific humidity contrasts ($\Delta\delta q_{\mathrm{a}}$ and Δq_{a}) act as the leading daytime drivers, particularly in the Tropics (Fig. 7a). $\Delta\delta q_{\mathrm{a}}$ shows consistently negative values in these zones (Supplementary Fig. s7), indicating relative urban drying (a widening urban–rural moisture gap) during HWs. Notably, a sharp drop in $\Delta\delta q_{\mathrm{a}}$ (becoming more negative) around sunrise (07 to 09 LT) coincides with a sharp increase in its positive SHAP contribution (enhanced ΔUHI), most clearly in the Tropical zone (Supplementary Fig. s7d). This aligns with the strong negative association shown in Fig. 5, where relative urban drying is associated with positive synergy. The high variability in the Tropical zone (Supplementary Fig. s1) underscores this moisture dependence: synergy is strong when the differential moisture absolute contrast is increasing ($\Delta\delta q_{\mathrm{a}}$ becomes more negative) during HWs but weak when gap decreases (Supplementary Fig. s7d).

Previous studies support this dependence on moisture. Variability in the urban-rural moisture contrast appears to control the strength of the synergy. Where background moisture is sufficient, the surface energy response to heat waves splits between rural and urban areas. Rural vegetation increases latent cooling through enhanced evapotranspiration, while urban areas remain water limited because impervious surfaces prevent infiltration and storage. This contrast widens the urban-rural moisture deficit ($\Delta\delta q_{\mathrm{a}} < 0$). Pyrgou et al.[34] demonstrated that this widening gap is not just a correlation. They argued that the urban-rural humidity contrasts act as the causal "regulator" of the interaction in Nicosia, Cyprus. Their regression analysis established a statistically significant dependence of UHI magnitude on the urban-rural humidity difference ($r = -0.42$), which is further connected to UHI-HW synergies by showing that heat waves push the humidity difference to more negative values. The heatwave-induced widening of the moisture gap was identified a key mechanism drives UHI intensification. By contrast, this synergistic pathway is absent in persistently saturated environments. Chew et al.[28] found no significant heatwave-UHI synergy in tropical Singapore. The consistently high background moisture prevented substantial change in the urban-rural humidity and soil moisture deficit ($\Delta\delta q_{\mathrm{a}} \approx 0$). Without a change in that deficit, the differential cooling due to latent heat flux needed to amplify the UHI cannot develop.

Interactions in moisture-limited climates
In moisture-limited climates, the scope for changes in evaporative cooling is small. Thus, advection and radiative processes show a stronger association (Fig. 7). Wind speed (ΔU10) is important during the day, peaking at its highest SHAP importance (21%) in the Arid zone. Sensible heat flux (SH) is more strongly associated at

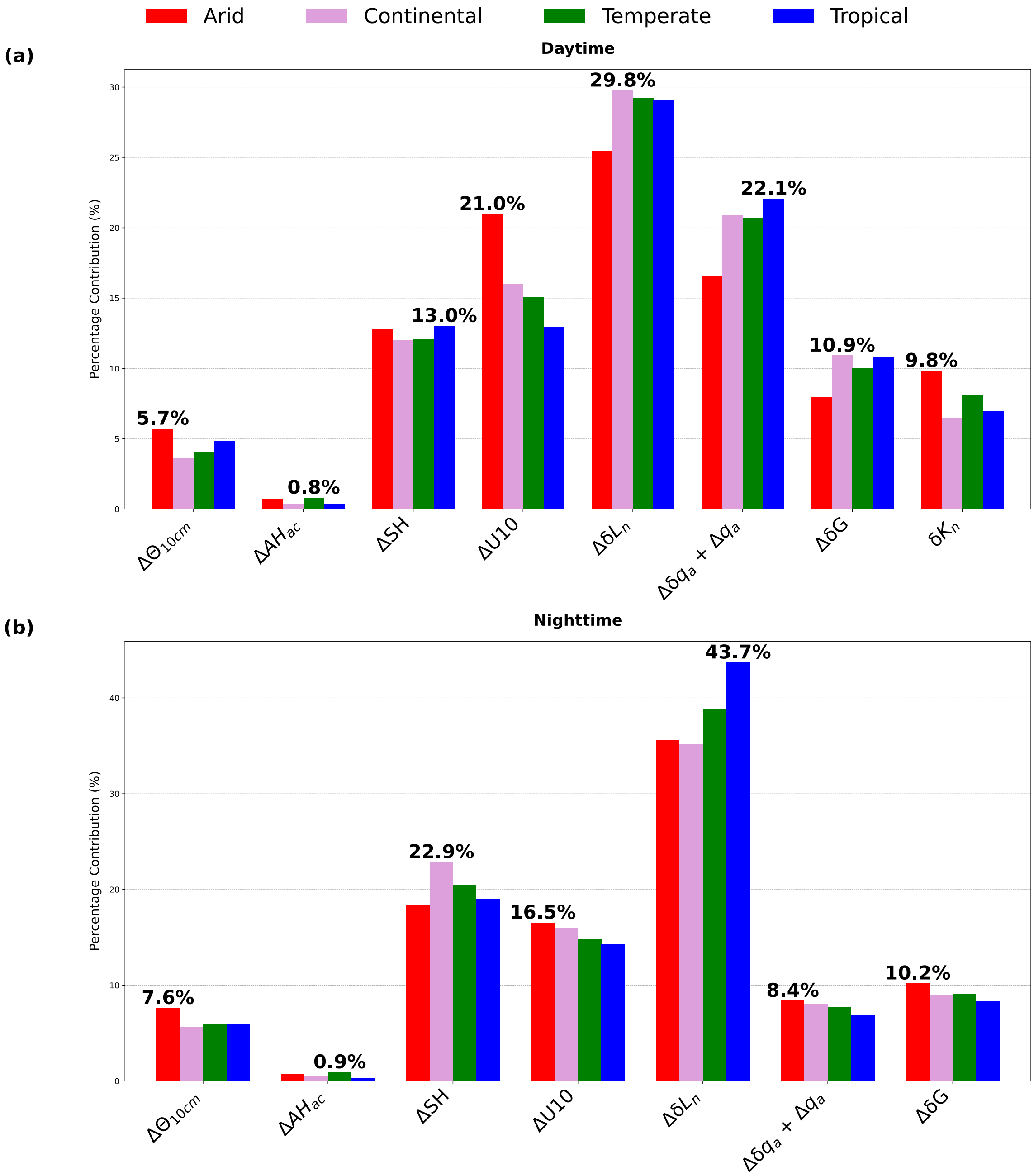

Fig. 7. Percentage Contribution of Feature Groups to Predicted ΔUHI, Stratified by Köppen-Geiger Climate Zones **for** (**a**) Daytime and (**b**) Nighttime. Bar chart illustrating the percentage contribution of each feature group to the predicted ΔUHI difference, categorized by Köppen-Geiger climate zones (Arid, Continental, Temperate, and Tropical). Percentage contributions are derived from aggregated SHAP values, indicating the relative importance of each feature group associated with ΔUHI within each climate region.

night, especially in Continental climates (23%), while humidity contributions decline. In Arid zones, the SHAP contribution of humidity (q_a) is the smallest (Supplementary Fig. s7a).

These patterns are corroborated by regional observations. Zhao et al.[7] found that in regions where both urban and rural surfaces are water-limited, the urban-rural humidity deficit does not widen during heat waves. With the evaporative cooling difference suppressed, the humidity contribution to ΔUHI is weaker. Synergy is primarily regulated by sensible heat flux and aerodynamic conditions. Li et al.[9] demonstrated that in Beijing, wind speed variations play a critical role, enhancing the UHI during heat waves by altering advective cooling. Similarly, Ngarambe et al.[36] observed that low wind speeds and atmospheric stagnation, often associated with heat waves, suppress horizontal advection, hindering the removal of urban heat and amplifying the role of sensible heat flux in driving the interaction.

Limitations and uncertainty analysis

It is important to note that the described method is not without limitations. Although we used a static 2015 urban land cover, which overestimates urban extent in earlier years, this should not bias the magnitude and geographical patterns of UHI-HW interactions. Constant urban properties are used because no reliable transient urban property dataset exists; however, we consider the UHI to be dominated by first-order urban-rural contrasts in biophysical properties, with second-order temporal variations playing a smaller role. Our representation of urban vegetation via the pervious canyon floor fraction captures first-order evaporative cooling effects but lacks explicit physiological responses (e.g., stomatal regulation), which may underestimate UHI enhancement during dry heatwaves when vegetation restricts transpiration. These model simplifications, while appropriate for global-scale analysis, imply that the ML-identified drivers reflect broad biophysical constraints rather than fine-scale intra-urban heterogeneity.

Despite these simplifications, CLM can capture regional variations in urban form and properties, vegetation effect, and anthropogenic heat variability. The focus of this study is on investigating how UHI-heat wave interactions vary across different climate backgrounds. The first-order urban characteristics that CLM5 does capture are sufficient for identifying these large scale patterns.

In our simulation setup, urban and rural lands within one grid cell receive the same atmospheric forcing. However, for large cities, urban and surrounding rural areas may be influenced by different atmospheric conditions, which could modify $\Delta\mathrm{UHI}$. This issue is secondary in this study because we focus on investigating the UHI-heatwave interactions driven by surface biophysical properties rather than by different atmospheric conditions. Although GSWP3 atmospheric forcing data demonstrate high quality[37], regional temperature biases are reported in mountainous regions, where air temperatures are biased high[38]. A systematic bias affecting both heat wave and non-heat wave periods similarly should not change our conclusions about UHI-heat wave interactions.

The interpretive limitations of SHAP[39] (capturing statistical association rather than physical causation) and the uncertainty quantification of our machine learning model (10-fold cross-validation demonstrating high stability with RMSE standard deviation < 1%) are detailed in the Supplementary Methods.

While these uncertainties may influence absolute magnitudes, our main conclusions about the relative patterns and mechanisms of UHI-HW interactions remain robust.

Conclusions

This study provides a global analysis of how urban heat islands and heat waves interact, using 29 years of Community Land Model simulations (1985–2013) across 3,648 urban grid cells. We quantified the synergy $\Delta\mathrm{UHI}$ and attributed it to biophysical variables using CatBoost and SHAP, achieving an RMSE of $0.0987°\mathrm{C}$. Our findings directly address three important questions about global UHI-HW interactions.

First, regarding where the strongest interactions occur: Heat waves intensify urban heat islands far more at night than by day. The global mean nighttime $\Delta\mathrm{UHI}$ is 0.27 ± $0.23\ °$C, while the daytime mean is 0.02 ± $0.22\ °$C. The diurnal cycle peaks near 06:00 LT and dips between 09:00 and 10:00. Daytime interactions are spatially heterogeneous. They can be neutral or negative along humid coasts and in major agricultural regions such as the United States Corn Belt and Western Europe. Nighttime effects are more uniform and stronger, with hotspots over the Indo Gangetic and North China Plains where $\Delta\mathrm{UHI}$ exceeds $0.8\ °$C. Continental climate zones show the highest mean synergy, whereas Tropical zones show the most significant variance.

Second, regarding the main contributors: Attribution identifies net longwave radiation as the dominant indicator of $\Delta\mathrm{UHI}$, accounting for 36.19% of the nighttime synergy and 27.19% during the day. This variable serves as a diagnostic signature of enhanced nocturnal heat release from urban structures. Secondary contributors depend on time of day: during the day, specific humidity contributes 22.46% and reflects amplified drying between urban and rural areas, expressed as negative $\Delta\delta q_a$, and 10-m wind speed contributes 15.76% at night; during the day, sensible heat flux contributes 11.96%, and at night, sensible heat flux ranks second at 20.34%. Mechanisms vary with climate. In moisture-rich tropical zones, humidity plays a significant role in the daytime interaction, and the magnitude depends on the depletion of rural soil moisture, which weakens evaporative cooling. Radiative and aerodynamic controls become more important in water-limited Arid and Continental zones, where wind speed and sensible heat flux become more dominant contributors alongside longwave radiation.

Third, regarding conditions that impact interactions: We find strong daytime $\Delta\mathrm{UHI}$ occurs when a large moisture gap between a moist rural area and a dry urban area is widened by further urban drying during HW ($\Delta\delta q_a < 0$), particularly in temperate or irrigated regions. Strong nighttime synergy occurs in Continental or Temperate with hot summer climates, where urban heat storage is prominent. $\Delta\mathrm{UHI}$ is maximized under stagnant, low-wind conditions typical of HWs, which hinder heat dispersion, amplify net longwave radiation differences ($\Delta\delta L_n > 0$), and maximize nocturnal $\Delta\mathrm{UHI}$.

These findings have direct implications for heat mitigation strategies. Mitigation should match local climate and the diurnal cycle, emphasizing moisture management and green infrastructure in humid regions, while prioritizing radiative cooling materials and enhanced ventilation in arid and continental settings. Future research should explore these interactions under climate change scenarios and investigate the role of urban morphology. The machine learning attribution framework offers a tractable tool for disentangling complex climate interactions and can be applied to other urban climate phenomena. As global urbanization continues and heat extremes intensify, understanding these synergistic effects becomes increasingly critical for protecting vulnerable urban populations.

Data availability
All data needed to evaluate the conclusions in the paper are present in the paper and the Supplementary Materials. Additional data related to this paper may be requested from the authors.

Received: 5 October 2025; Accepted: 21 January 2026
Published online: 14 February 2026

References
1. Roxon, J., Ulm, F. J. & Pellenq, R. J. M. Urban heat island impact on state residential energy cost and CO2 emissions in the United States. *Urban Clim.* **31**, 100546 (2020).
2. Vicedo-Cabrera, A. M. et al. The burden of heat-related mortality attributable to recent human-induced climate change. *Nat. Clim. Chang.* **11**, 492–500 (2021).
3. Zander, K. K., Botzen, W. J., Oppermann, E., Kjellstrom, T. & Garnett, S. T. Heat stress causes substantial labour productivity loss in Australia. *Nat. Clim. Chang.* **5**, 647–651 (2015).
4. Kong, J., Zhao, Y., Carmeliet, J. & Lei, C. Urban heat island and its interaction with heatwaves: A review of studies on mesoscale. *Sustainability* **13**, 10923 (2021).
5. Cui, F. et al. Interactions between the summer urban heat islands and heat waves in Beijing during 2000–2018. *Atmos. Res.* **291**, 106813 (2023).
6. Park, K., Baik, J.-J., Jin, H.-G. & Tabassum, A. Changes in urban heat island intensity with background temperature and humidity and their associations with near-surface thermodynamic processes. *Urban Clim.* **58**, 102191 (2024).
7. Zhao, L. et al. Interactions between urban heat islands and heat waves. *Environ. Res. Lett.* **13**, 034003 (2018).
8. Khan, H. S., Paolini, R., Santamouris, M. & Caccetta, P. Exploring the synergies between urban overheating and heatwaves (HWs) in western sydney. *Energies* **13**, 470 (2020).
9. Li, D., Sun, T., Liu, M., Wang, L. & Gao, Z. Changes in wind speed under heat waves enhance urban heat islands in the beijing metropolitan area. *J. Appl. Meteorol. Climatol.* **55**, 2369–2375 (2016).
10. Shu, C., Gaur, A., Lacasse, M. & Wang, L. L. Interaction between the urban heat island effect and the occurrence of heatwaves: Comparison of days with and without heatwaves, in *International Conference on Building Energy and Environment* 3019–3028 (Springer, 2022).
11. Tabassum, A., Park, K., Seo, J. M., Han, J.-Y. & Baik, J.-J. Characteristics of the urban heat island in dhaka, bangladesh, and its interaction with heat waves. *Asia-Pac. J. Atmos. Sci.* **60**, 479–493 (2024).
12. Li, D. et al. Contrasting responses of urban and rural surface energy budgets to heat waves explain synergies between urban heat islands and heat waves. *Environ. Res. Lett.* **10**, 054009 (2015).
13. Zhang, K. et al. Increased heat risk in wet climate induced by urban humid heat. *Nature* **617**, 738–742 (2023).
14. Venter, Z. S., Chakraborty, T. & Lee, X. Crowdsourced air temperatures contrast satellite measures of the urban heat island and its mechanisms. *Sci. Adv.* **7**, eabb9569 (2021).
15. Danabasoglu, G. et al. The community earth system model version 2 (CESM2). *J. Adv. Model. Earth Syst.* **12**, e2019-001916 (2020).
16. Oleson, K. *et al.* Technical description of the community land model (clm). *NCAR Technical Note* (2004).
17. Lawrence, D. M. et al. The community land model version 5: Description of new features, benchmarking, and impact of forcing uncertainty. *J. Adv. Model. Earth Syst.* **11**, 4245–4287 (2019).
18. Gao, J. & O'Neill, B. C. Mapping global urban land for the 21st century with data-driven simulations and shared socioeconomic pathways. *Nat. Commun.* **11**, 2302 (2020).
19. Jackson, T. L., Feddema, J. J., Oleson, K. W., Bonan, G. B. & Bauer, J. T. Parameterization of urban characteristics for global climate modeling. *Ann. Assoc. Am. Geogr.* **100**, 848–865 (2010).
20. Zhao, L., Lee, X., Smith, R. B. & Oleson, K. Strong contributions of local background climate to urban heat islands. *Nature* **511**, 216–219 (2014).
21. Lipson, M. J. et al. Evaluation of 30 urban land surface models in the urban-plumber project: Phase 1 results. *Q. J. R. Meteorol. Soc.* **150**, 126–169 (2024).
22. Oleson, K. & Feddema, J. Parameterization and surface data improvements and new capabilities for the community land model urban (clmu). *J. Adv. Model. Earth Syst.* **12**, e2018MS001586 (2020).
23. Garuma, G. F. How the interaction of heatwaves and urban heat islands amplify urban warming. *Adv. Environ. Eng. Res.* **3**, 1–1 (2022).
24. Lee, X. Eq. 2.32, in *Fundamentals of Boundary-Layer Meteorology* (Springer, 2023).
25. An, N. et al. An observational case study of synergies between an intense heat wave and the urban heat island in Beijing. *J. Appl. Meteorol. Climatol.* **59**, 605–620 (2020).
26. Jiang, S., Lee, X., Wang, J. & Wang, K. Amplified urban heat islands during heat wave periods. *J. Geophys. Res. Atmos.* **124**, 7797–7812 (2019).
27. Park, K., Jin, H.-G. & Baik, J.-J. Contrasting interactions between urban heat islands and heat waves in Seoul, South Korea, and their associations with synoptic patterns. *Urban Clim.* **49**, 101524 (2023).
28. Chew, L. W., Liu, X., Li, X.-X. & Norford, L. K. Interaction between heat wave and urban heat island: A case study in a tropical coastal city. *Singapore Atmos. Res.* **247**, 105134 (2021).
29. Kumar, R. & Mishra, V. Decline in surface urban heat island intensity in India during heatwaves. *Environ. Res. Commun.* **1**, 031001 (2019).
30. Scott, A. A., Waugh, D. W. & Zaitchik, B. F. Reduced Urban Heat Island intensity under warmer conditions. *Environ. Res. Lett.* **13**, 064003 (2018).
31. Rogers, C. D., Gallant, A. J. & Tapper, N. J. Is the urban heat island exacerbated during heatwaves in southern Australian cities?. *Theoret. Appl. Climatol.* **137**, 441–457 (2019).
32. Beck, H. E. et al. High-resolution (1 km) Köppen-Geiger maps for 1901–2099 based on constrained CMIP6 projections. *Sci. Data* **10**, 724 (2023).
33. Lee, X. Eq. 2.29, in *Fundamentals of Boundary-Layer Meteorology* (Springer, 2023).
34. Pyrgou, A., Hadjinicolaou, P. & Santamouris, M. Urban-rural moisture contrast: Regulator of the urban heat island and heatwaves' synergy over a mediterranean city. *Environ. Res.* **182**, 109102 (2020).
35. Li, D. & Bou-Zeid, E. Synergistic interactions between urban heat islands and heat waves: The impact in cities is larger than the sum of its parts. *J. Appl. Meteorol. Climatol.* **52**, 2051–2064 (2013).
36. Ngarambe, J., Nganyiyimana, J., Kim, I., Santamouris, M. & Yun, G. Y. Synergies between urban heat island and heat waves in Seoul: The role of wind speed and land use characteristics. *PLoS ONE* **15**, e0243571 (2020).
37. Ma, X. & Wang, A. Evaluation and uncertainty analysis of the land surface hydrology in ls3mip models over China. *Earth Space Sci.* **11**, e2023EA003391 (2024).
38. Ménard, C. B. et al. Meteorological and evaluation datasets for snow modelling at ten reference sites: description of in situ and bias-corrected reanalysis data. *Earth Syst. Data Discuss.* **2019**, 1–34 (2019).

39. Ghorbany, S., Hu, M., Yao, S. & Wang, C. Towards a sustainable urban future: A comprehensive review of urban heat island research technologies and machine learning approaches. *Sustainability* **16**, 4609 (2024).

Author contributions
J.G. designed the study, performed the analysis and wrote the manuscript. K.Z. provided guidance on study design and contributed to manuscript revision. X.L. contributed to ideas and manuscript revision.

Funding
The authors received no specific financial support for the research, authorship, and/or publication of this article.

Declarations

Competing interests
The authors declare no competing interests.

Additional information
Supplementary Information The online version contains supplementary material available at https://doi.org/10.1038/s41598-026-37372-7.

Correspondence and requests for materials should be addressed to K.Z.

Reprints and permissions information is available at www.nature.com/reprints.

Publisher's note Springer Nature remains neutral with regard to jurisdictional claims in published maps and institutional affiliations.